https://doi.org/10.1038/s41586-018-0339-0

# Photoswitching topology in polymer networks with metal–organic cages as crosslinks

Yuwei Gu[1], Eric A. Alt[1], Heng Wang[2], Xiaopeng Li[2], Adam P. Willard[1] & Jeremiah A. Johnson[1]*

**Polymer networks can have a range of desirable properties such as mechanical strength, wide compositional diversity between different materials, permanent porosity, convenient processability and broad solvent compatibility[1,2]. Designing polymer networks from the bottom up with new structural motifs and chemical compositions can be used to impart dynamic features such as malleability or self-healing, or to allow the material to respond to environmental stimuli[3–8]. However, many existing systems exhibit only one operational state that is defined by the material's composition and topology[3–6]; or their responsiveness may be irreversible[7,9,10] and limited to a single network property[11,12] (such as stiffness). Here we use cooperative self-assembly as a design principle to prepare a material that can be switched between two topological states. By using networks of polymer-linked metal–organic cages in which the cages change shape and size on irradiation, we can reversibly switch the network topology with ultraviolet or green light. This photoswitching produces coherent changes in several network properties at once, including branch functionality, junction fluctuations, defect tolerance, shear modulus, stress-relaxation behaviour and self-healing. Topology-switching materials could prove useful in fields such as soft robotics and photo-actuators and also provide model systems for fundamental polymer physics studies.**

The topological connections between polymer network strands and junctions—including branch functionality, cyclic defects, entanglements and density fluctuations—have long been implicated in dictating the bulk properties of polymer networks[13]. With the advent of new synthetic methods and tools for polymer network characterization[14–16], recent studies have revealed that network topology, as one of the few global parameters for polymer networks, plays a critical role in determining material properties such as elasticity[17], the gel point[18], network dynamics[15] and degree of defect tolerance[5]. Here we propose and examine topology switching as a strategy to develop dynamic and stimuli-responsive materials in which multiple aspects of the materials' properties are regulated coherently.

We hypothesized that polymer metal–organic cage (polyMOC) networks[5,19], which are a class of materials formed from the metallosupramolecular assembly of discrete MOCs connected to polymer chains, could provide a route to topology-switchable materials (Fig. 1a). In polyMOCs, the network junctions are nanoscale metal$_x$ligand$_y$ ($M_xL_y$) cages of defined shape and stoichiometry[20,21]; the MOC structure defines the polyMOC topology and bulk properties. Inspired by recent developments in modulating MOC conformation in a stimuli-responsive fashion[22,23], we began our investigation with the design and synthesis of a poly(ethylene glycol)-based polymer ligand (Fig. 1b), which features two bis-pyridyl dithienylethene (DTE) groups. We hypothesized that, in the presence of $Pd^{2+}$, these ligands would form MOCs that could be reversibly photoswitched between small $Pd_3L_6$ rings and large $Pd_{24}L_{48}$ rhombicuboctahedra by irradiating with green and ultraviolet (UV) light, respectively[23]. Before embarking on polyMOC synthesis using polymer ligands, we conducted model studies with a non-polymeric bis-pyridyl DTE-derivative ligand to confirm the photoswitching capability of these DTE derivatives (Extended Data Fig. 1).

When 1 equivalent of the open-form polymer ligand (o-PL) was mixed with 1 equivalent of $Pd(CH_3CN)_4(BF_4)_2$ in $CH_3CN$ (25.1 mM $Pd^{2+}$), a dark-brown gel formed (named o-gel). After annealing at 60 °C for 4 h to enable equilibration of the network junctions, the o-gel was characterized with oscillatory rheometry (Fig. 2a, Extended Data Fig. 2a). The material displayed elastic behaviour at all frequencies with a storage modulus ($G'$) of about 8.3 kPa at 10 rad $s^{-1}$. Irradiation of the o-gel with UV light for 5 h at 60 °C produced a dark blue material, which we call c-gel (for closed-form), with a nearly doubled $G'$ (Fig. 2a). The shear loss modulus ($G''$) of the c-gel (Extended Data Fig. 2b) was slightly higher than that of the o-gel at the measured frequencies (1–100 rad $s^{-1}$). We attribute such behaviour to the presence of a greater number of topological defects (for example cyclic defects) in the c-gel—a characteristic feature for polyMOC gels with high branch functionality, $f$ (ref. [5]). A sample of the c-gel prepared directly from pre-synthesized closed-form polymer ligand (c-PL) and $Pd^{2+}$ displayed nearly identical frequency behaviour (Extended Data Fig. 2d), which suggests that the observed changes in mechanical properties on conversion of the o-gel to c-gel are due to photoswitching of the DTE-containing MOC junctions. Finally, exposure of the c-gel to green light for 5 h at 60 °C regenerated the o-gel with only a slight decrease in stiffness compared with the original o-gel ($G' = 7.8$ kPa; Fig. 2a, Extended Data Fig. 2c). Notably, the o-gel and c-gel have the same molar concentration of polymer strands and Pd atoms. Although the magnitude of the change in $G'$ demonstrated here is relatively small (a factor of 1.7), in conventional supramolecular materials based on point interactions, the o-gel and c-gel would be expected to have the same $G'$; the hierarchical nature of polyMOCs enables access to two distinct topological states with different densities of elastically effective strands, cyclic defects and junction fluctuations, which leads to different $G'$.

Small-angle X-ray scattering (SAXS) was used to confirm that the mechanical changes observed above were due to changes in the MOC structure within the o-gel and c-gel (Fig. 2b, c). The scattering curve for the o-gel shows a broad peak at scattering vector $q = 0.080$ Å$^{-1}$ and a weak peak at $q = 0.729$ Å$^{-1}$ (Fig. 2b, inset). The latter peak agrees with the form factor of a uniform spherical particle with radius of 0.79 nm. We attribute this peak to scattering from $Pd_3L_6$ MOCs within the o-gel. The low-$q$ SAXS peak, which corresponds to a $d$-spacing of about 7.85 nm, was assigned as the average distance between MOCs linked by polymer chains.

The SAXS curve for the c-gel displayed a sharpened peak shifted to lower $q$ than for the o-gel, as well as five new peaks in the high-$q$ regime (Fig. 2b, Extended Data Fig. 3a). The latter peaks were best fitted by the form factor of a uniform spherical particle with a 2.9-nm radius (Extended Data Fig. 3b), which agrees remarkably well with the analogous measurement by diffusion ordered NMR spectroscopy (DOSY) (3.1 nm; Extended Data Fig. 1c). The low-$q$ SAXS peak for the c-gel corresponds to a $d$-spacing of 11.9 nm; this increased distance between MOCs compared with the o-gel reflects the fact that the larger

[1]Department of Chemistry, Massachusetts Institute of Technology, Cambridge, MA, USA. [2]Department of Chemistry, University of South Florida, Tampa, FL, USA. *e-mail: jaj2109@mit.edu



© 2018 Springer Nature Limited. All rights reserved.

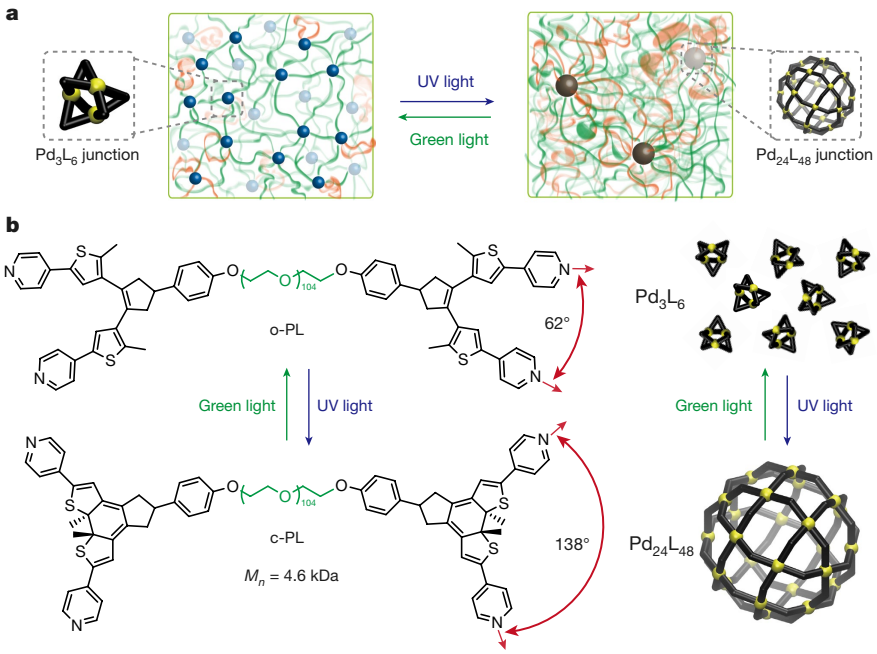


**Fig. 1 | Design of polyMOCs with photoswitchable topology.** **a**, Schematic illustration of photo-regulated interconversion between two different network topologies. Photoresponsive MOCs are introduced as junctions within polyMOCs. On UV irradiation, the MOC rearranges its structure from $Pd_3L_6$ to $Pd_{24}L_{48}$. Consequently, the network topology (for example, average branch functionality and cyclic defects) is altered. Reversal of the MOC structure with green light regenerates the original network topology. **b**, Chemical structure of the photoresponsive polymer ligand and a schematic of MOC interconversion. The DTE moiety undergoes electrocyclic ring-closure and ring-opening on UV and green-light irradiation, respectively. Note that the ring-closure reaction produces a racemic mixture of *trans*-ring-closed products. Photoinduced ring-closure/opening leads to a change of bite angle between the two attached pyridine groups. Hence, the open-form (o-PL) and closed-form (c-PL) polymer ligands form small $Pd_3$(o-PL)$_6$ and large $Pd_{24}$(c-PL)$_{48}$ MOCs, respectively, in the presence of $Pd^{2+}$. The existence of many diastereomeric cage structures does not seem to inhibit the assembly process.

MOCs in the c-gel must be further apart to maintain a constant Pd concentration. The sharpening and increased intensity of the low-$q$ SAXS peak for the c-gel is another sign that this material possesses uniform Pd-rich regions ($Pd_{24}L_{48}$ MOCs).

We carried out simulations of $Pd_3L_6$ (o-gel) and $Pd_{24}L_{48}$ (c-gel) polyMOC gels (25.1 mM $Pd^{2+}$) using a coarse-grained model of dynamic network topology to probe the topology of our materials in more detail (Fig. 2d, e, Extended Data Figs. 5, 6). Specifically, the model was used to compute the density of loop defects and the average network branch functionality ($\bar{f}$).

Whereas 40.3% of the strands in the simulated o-gel were primary loops (that is, both ends of the strand were connected to the same $Pd_3L_6$ MOC; red strands in Fig. 2d), a remarkable 74.2% of the strands in the simulated c-gel were primary loops (red strands in Fig. 2e). Despite this increase in elastically inactive primary loops, as noted above, $G'$ for the c-gel was 1.7 times that for the o-gel. In other words, on switching topology, the degree to which these materials could tolerate defects is changed (the c-gel can withstand more defects than the o-gel). Aiming to increase $\Delta G'$ further, we prepared the o-gel′ by replacing 15% of o-PL in the o-gel with free ligand o-L (these free ligands represent elastically inactive 'defects'), as shown in Fig. 2f. Because of its low degree of defect tolerance, the o-gel′ has much lower $G'$ than the unmodified o-gel (about 1.2 kPa versus about 8.3 kPa). On irradiating with UV light, topology switching (see Extended Data Fig. 4d for SAXS data) results in a highly defect-tolerant state (c-gel′), increasing $G'$ by an order of magnitude (from about 1.2 kPa to about 9.8 kPa; Fig. 2f, Extended Data Fig. 4a, b). The switching process was confirmed to be reversible (Fig. 2f, Extended Data Fig. 4c). Given such a large and reversible $\Delta G'$, we anticipate that topology-switching materials could find applications in fields such as soft robotics and photo-actuators. Moreover, the incorporation of free ligand offers a general yet simple strategy to introduce functional moieties into polyMOC junctions. As branch functionality and junction size are altered considerably on switching topology, the possible number of functional moieties that can be confined in a MOC is increased or decreased[24]; this could prove useful for reversible encapsulation and release of small molecules, as well as for responsive materials based on multivalent interactions[25].

The simulated $\bar{f}$ were compared with experimental results. To calculate experimental $\bar{f}$ from measured $G'$ values, two network models—an affine network and a phantom network—were applied, which assume different degrees of network junction fluctuation. As the network topology switched from the o-gel to the c-gel, the local mass density around each network junction was greatly increased. Consequently, our results (Extended Data Fig. 6) indicate that the ability of the network junctions to fluctuate around average positions was diminshed, which corresponds to a reversible phantom-to-affine transition in polymer networks. Because the difference between a phantom and an affine network forms the basis of a thorough understanding of rubber elasticity[2], we anticipate that the reversible phantom-to-affine transition achieved through topology switching may be an ideal model system in which to examine these two network models experimentally.

Owing to cooperative effects, the metal–ligand bonds in large MOCs are often much less dynamic than the same bonds in smaller complexes[26]. Thus, we expect the o-gel to be much more dynamic than the c-gel, which provides the ability to switch network dynamics through topology switching. Measurements of swelling in excess $CH_3CN$ solvent (Fig. 3a) support our hypothesis: the o-gel absorbed $102 \pm 13$ times its own weight in $CH_3CN$ after 5 days and completely dissolved after 20 days, whereas the c-gel absorbed $14 \pm 6$ times its own weight in $CH_3CN$ after 5 days and did not swell further over 20 days.

Stress-relaxation measurements were conducted to quantitatively evaluate the dynamics of the o-gel and c-gel as a function of temperature (Fig. 3b, c, respectively); characteristic relaxation times $\tau$ were obtained by fitting experimental data to the Kohlrausch model. For both the o-gel and c-gel, $\tau$ decreased as temperature increased, owing to thermally accelerated ligand exchange. More importantly, at the same temperature, $\tau$ for the c-gel was consistently about an order of magnitude larger than for the o-gel. In addition, $\tau$ for the o-gel at


© 2018 Springer Nature Limited. All rights reserved.

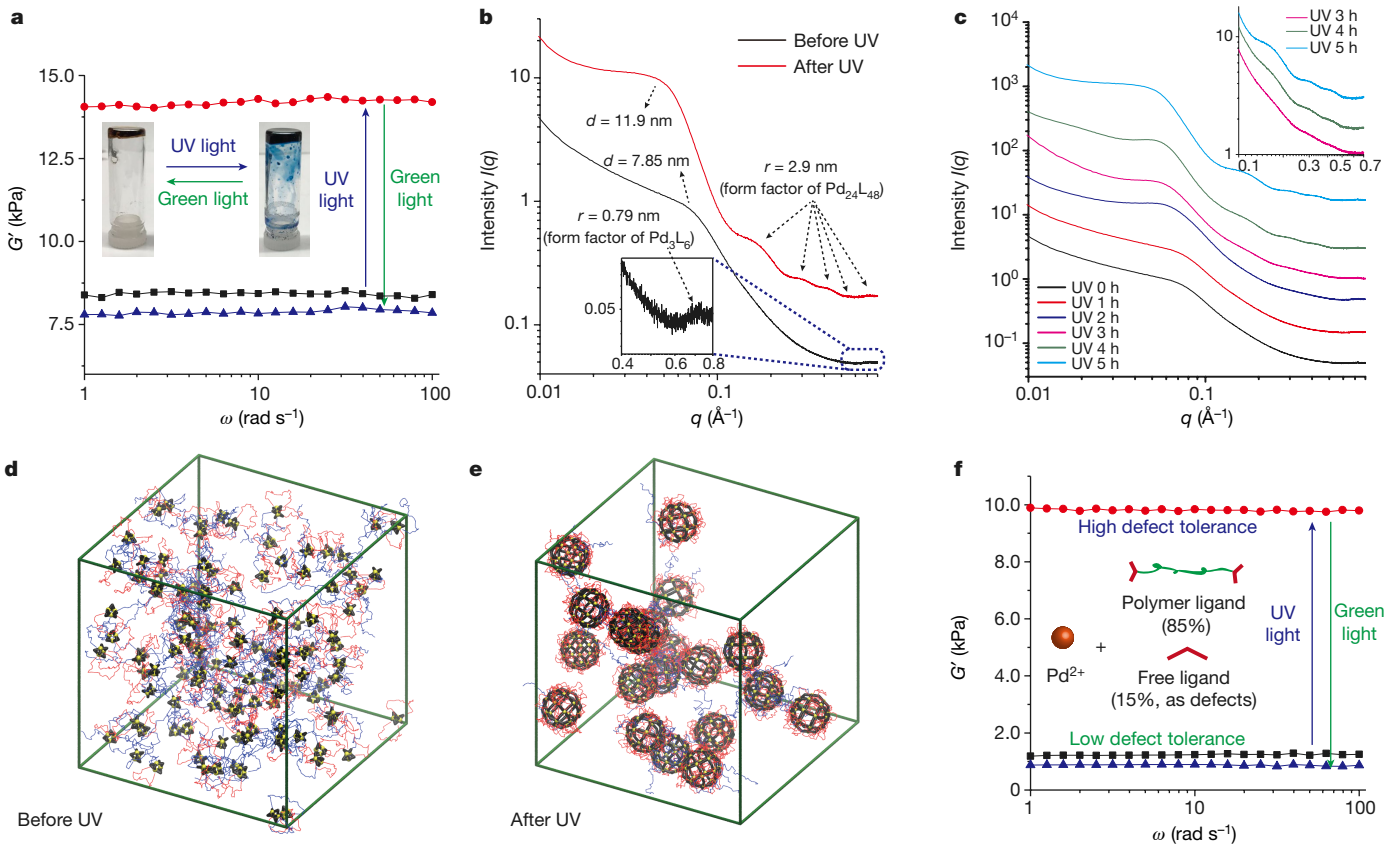


**Fig. 2 | Photoswitching of polyMOC topology. a**, A brown polyMOC (o-gel) was formed by mixing o-PL and $Pd(CH_3CN)_4(BF_4)_2$ in $CH_3CN$ (25.1 mM). The shear storage modulus ($G'$) of the o-gel was 8.3 kPa (black curve). UV irradiation of the o-gel at 60 °C for 5 h produced a blue material (c-gel) with $G' = 14.1$ kPa (red curve). Irradiation with green light regenerated the o-gel with nearly the same $G'$ (blue curve). The slight decrease in $G'$ on regeneration of the o-gel is believed to be due to a small amount of ligand photodegradation. **b**, SAXS curves for polyMOCs before (black curve) and after (red curve) UV irradiation. The $d$-spacing in the low-$q$ regime is assigned as the average distance between MOC junctions. The high-$q$ peaks correspond to form factors of $Pd_3$(o-PL)$_6$ (inset) and $Pd_{24}$(c-PL)$_{48}$. **c**, SAXS curves over the course of UV irradiation. Inset, zoom-in of the high-$q$ regime of the SAXS curves. The form factor corresponding to $Pd_{24}$(c-PL)$_{48}$ emerges over time, providing direct evidence for the transition of network topology. **d**, Snapshot of the simulated o-gel. Primary loop strands are shown in red. **e**, Snapshot of the simulated c-gel. Primary loop strands are shown in red. **f**, Topology switching produces a marked switch in the degree of defect tolerance. By replacing 15% o-PL with o-L, we were able to switch $G'$ by one order of magnitude, from about 1 kPa to about 10 kPa, on switching the topology. Each experimental curve in **a**, **b**, **c** and **f** shows a representative result of at least three measurements, which showed excellent reproducibility with a relative standard deviation of less than 5%.

room temperature ($\tau = 555$ s) was less than that for the c-gel at 60 °C ($\tau = 1{,}085$ s). Thanks to topology switching, the static properties ($G'$) and dynamic properties ($\tau$) of this material could be simultaneously switched, both by one order of magnitude. This design principle opens many potential applications, such as soft adhesives, or biomaterials for adaptive cell culture that can reversibly switch stiffness and stress relaxation rate, both of which have been shown to be essential to regulate stem-cell fate and cell proliferation[27,28].

These differences in relaxation kinetics between the o-gel and c-gel should translate to unique topology-dependent self-healing behaviours; the slow exchange kinetics of the c-gel should make it less able to heal. To test this hypothesis, samples of the o-gel and c-gel were cut into two pieces and placed in contact; considering the difference in measured relaxation timescales between the o-gel and c-gel, the self-healing condition was chosen as 4 h at 40 °C. After 4 h, the o-gel was completely healed with no visible damage at the interface, whereas the c-gel remained in two separate pieces. In addition, our polyMOC could be switched from the healable state (o-gel) to the non-healable state (c-gel) and back (Fig. 3d).

Most existing self-healing materials rely on fast bond exchange in the healable state. Although such fast bond exchange provides self-healing properties, the same mechanism leads to low mechanical robustness and considerable material deformation on loading, which makes self-healing materials unsuitable for many applications. Topology switching is a general way to break this limitation. It allows a single material to be operated in one topological state (c-gel) that is mechanically robust and suitable for heavier-duty applications; if the material is damaged or needs to be re-processed, one can simply switch its topology to the self-healable state (o-gel) to heal or process the material, and then switch back to the operation state[29].

To study the fatigue behaviour of our materials, we measured $G'$ over several cycles of switching between the o-gel and c-gel using two sets of irradiation conditions. As shown in Fig. 4a (black line), when the polyMOC was cycled between exposure to UV light for 5 h at 60 °C and green light for 5 h at 60 °C, the material displayed elastic behaviour in both topological states for seven cycles. When cycled at lower temperature (45 °C) and longer irradiation time (12 h), the material lost its mechanical integrity after three cycles (Fig. 4a, red curve). These data are indicative of photoinduced degradation, probably of the DTE-containing ligands, because related DTE derivatives are known to degrade under extended UV irradiation[30]. SAXS was used to probe the fatigue mechanism of our polyMOCs in more detail. The scattering profiles for the o-gel and c-gel did not noticeably change after three switching cycles (Fig. 4b); however, the scattering profiles after seven switching cycles (green and yellow curves in Fig. 4b) no longer possess the MOC form factors, suggesting that UV-induced DTE degradation disrupted uniform MOC formation. The presence of low-$q$ SAXS peaks after seven cycles suggests the presence of metal–ligand clusters


© 2018 Springer Nature Limited. All rights reserved.

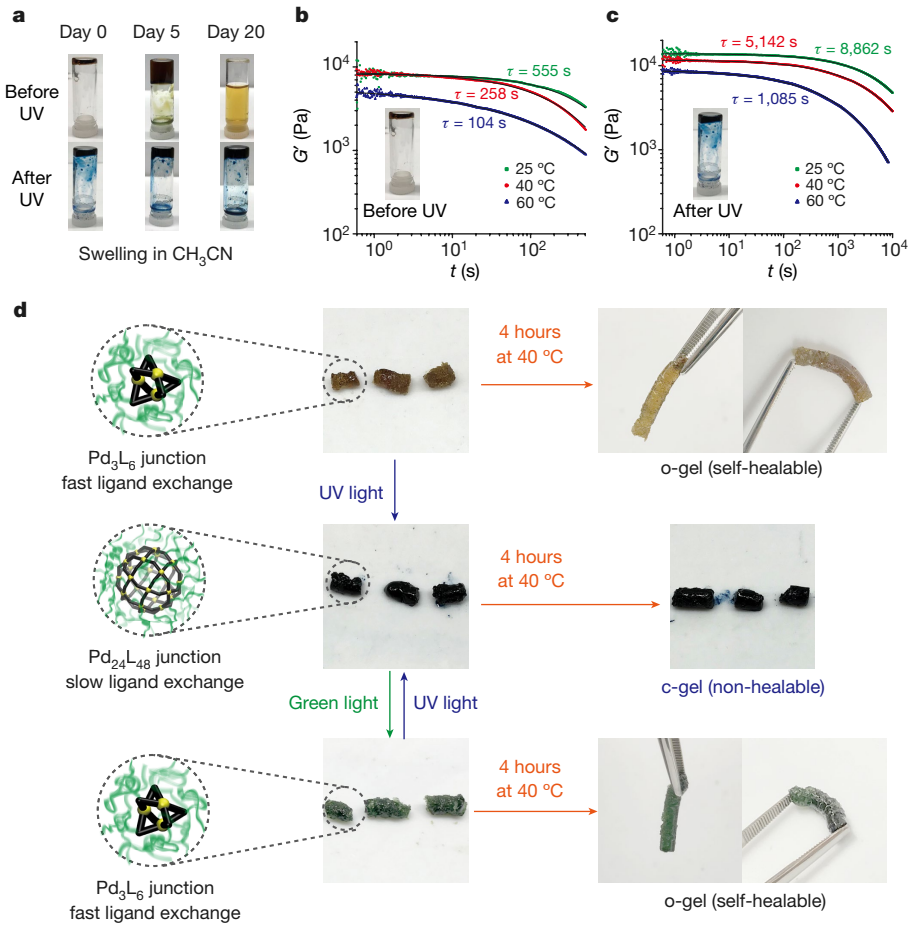


**Fig. 3 | Photoswitching topology leads to tunable network dynamics.** **a**, Swelling before (o-gel) and after (c-gel) UV irradiation. **b**, Stress-relaxation curves at various temperatures for the o-gel. Curves were fitted with the Kohlrausch model to provide the characteristic relaxation times $\tau$. Symbols, raw data; solid lines, fitted data. **c**, Stress-relaxation curves at various temperatures for the c-gel. Each experimental curve in **b** and **c** shows a representative result of at least three measurements, which showed excellent reproducibility with a relative standard deviation of less than 5%. **d**, Photographs of self-healing experiments, which demonstrate that the o-gel undergoes self-healing whereas the c-gel does not.

of ill-defined structure; these clusters may still provide mechanical robustness to the material.

To elucidate the fatigue mechanism in more detail, $\bar{f}$ values were calculated based on $G'$ values measured over several switching cycles (Fig. 4c). After seven cycles, the c-gel still possesses a very high $\bar{f}$ value ($6.26 \pm 0.51$). In contrast, $\bar{f}$ for the o-gel after seven cycles ($2.22 \pm 0.07$) is close to the $f = 2$ limit at which the sol–gel transition starts to occur. To model the extent of UV-induced DTE degradation, dynamic

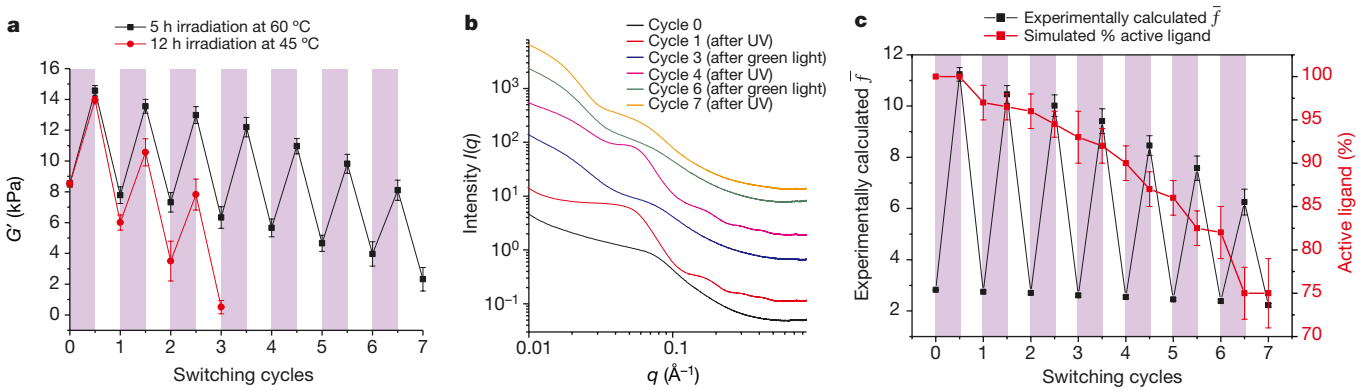


**Fig. 4 | Fatigue properties.** **a**, Shear modulus $G'$ over multiple topology switching cycles. Each switching cycle includes UV irradiation (purple regions) followed by green-light irradiation (white regions). Two different irradiation schemes were applied for each UV or green-light irradiation. Higher temperature enabled reduction of the irradiation time, which gave improved fatigue resistance. Error bars represent the standard deviation of three measurements. **b**, SAXS curves for topology switching cycles. Each experimental curve shows a representative result of at least three measurements, which showed excellent reproducibility with a relative standard deviation of less than 5%. **c**, Average branch functionality ($\bar{f}$) calculated on the basis of $G'$ over multiple switching cycles (black curves), and simulation results based on the experimentally calculated $\bar{f}$ for the ligand degradation profile over multiple switching cycles (red curves). In the calculation of $\bar{f}$, the c-gel and o-gel are treated as affine and phantom networks, respectively. Error bars represent the standard deviation of three measurements.



© 2018 Springer Nature Limited. All rights reserved.

network topology simulations were used to compute $\overline{f}$ as a function of the percentage of active ligand within these polyMOCs (Extended Data Fig. 7); $\overline{f}$ values obtained from experiment were then translated to a ligand degradation profile (Fig. 4c). From these data, we estimate that 25% of the DTE-based ligand was degraded over seven cycles. This result is consistent with the degradation profile of free ligand obtained by $^{1}$H NMR (Extended Data Fig. 8).

## Online content

Any Methods, including any statements of data availability and Nature Research reporting summaries, along with any additional references and Source Data files, are available in the online version of the paper at https://doi.org/10.1038/s41586-018-0339-0.

Received: 4 February 2018; Accepted: 16 May 2018;
Published online 18 July 2018.

1. Osada, Y. & Gong, J.-P. Soft and wet materials: polymer gels. *Adv. Mater*. **10**, 827–837 (1998).
2. Rubinstein, M. & Colby, R. H. *Polymer Physics* (Oxford Univ. Press, Oxford, 2003).
3. Chen, X. et al. A thermally re-mendable cross-linked polymeric material. *Science* **295**, 1698–1702 (2002).
4. Burnworth, M. et al. Optically healable supramolecular polymers. *Nature* **472**, 334–337 (2011).
5. Zhukhovitskiy, A. V. et al. Highly branched and loop-rich gels via formation of metal–organic cages linked by polymers. *Nat. Chem*. **8**, 33–41 (2016).
6. Röttger, M. et al. High-performance vitrimers from commodity thermoplastics through dioxaborolane metathesis. *Science* **356**, 62–65 (2017).
7. Cangialosi, A. et al. DNA sequence-directed shape change of photopatterned hydrogels via high-degree swelling. *Science* **357**, 1126–1130 (2017).
8. Vatankhah-Varnosfaderani, M. et al. Mimicking biological stress–strain behaviour with synthetic elastomers. *Nature* **549**, 497–501 (2017).
9. Kloxin, A. M., Kasko, A. M., Salinas, C. N. & Anseth, K. S. Photodegradable hydrogels for dynamic tuning of physical and chemical properties. *Science* **324**, 59–63 (2009).
10. Ramirez, A. L. B. et al. Mechanochemical strengthening of a synthetic polymer in response to typically destructive shear forces. *Nat. Chem*. **5**, 757–761 (2013).
11. Scott, T. F., Schneider, A. D., Cook, W. D. & Bowman, C. N. Photoinduced plasticity in cross-linked polymers. *Science* **308**, 1615–1617 (2005).
12. Rosales, A. M. & Anseth, K. S. The design of reversible hydrogels to capture extracellular matrix dynamics. *Nat. Rev. Mater*. **1**, 15012 (2016).
13. Flory, P. J. Network topology and the theory of rubber elasticity. *Br. Polym. J*. **17**, 96–102 (1985).
14. Zhou, H. et al. Counting primary loops in polymer gels. *Proc. Natl Acad. Sci. USA* **109**, 19119–19124 (2012).
15. Noda, Y., Hayashi, Y. & Ito, K. From topological gels to slide-ring materials. *J. Appl. Polym. Sci*. **131**, 40509 (2014).
16. Di Lorenzo, F. & Seiffert, S. Nanostructural heterogeneity in polymer networks and gels. *Polym. Chem*. **6**, 5515–5528 (2015).
17. Zhong, M., Wang, R., Kawamoto, K., Olsen, B. D. & Johnson, J. A. Quantifying the impact of molecular defects on polymer network elasticity. *Science* **353**, 1264–1268 (2016).
18. Wang, R., Lin, T.-S., Johnson, J. A. & Olsen, B. D. Kinetic Monte Carlo simulation for quantification of the gel point of polymer networks. *ACS Macro Lett*. **6**, 1414–1419 (2017).
19. Wang, Y. et al. Star polyMOCs with diverse structures, dynamics, and functions by three-component assembly. *Angew. Chem. Int. Ed*. **56**, 188–192 (2017).
20. Leininger, S., Olenyuk, B. & Stang, P. J. Self-assembly of discrete cyclic nanostructures mediated by transition metals. *Chem. Rev*. **100**, 853–908 (2000).
21. Harris, K., Fujita, D. & Fujita, M. Giant hollow $M_nL_{2n}$ spherical complexes: structure, functionalisation and applications. *Chem. Commun*. **49**, 6703–6712 (2013).
22. McConnell, A. J., Wood, C. S., Neelakandan, P. P. & Nitschke, J. R. Stimuli-responsive metal–ligand assemblies. *Chem. Rev*. **115**, 7729–7793 (2015).
23. Han, M. et al. Light-controlled interconversion between a self-assembled triangle and a rhombicuboctahedral sphere. *Angew. Chem. Int. Ed*. **55**, 445–449 (2016).
24. Ueda, Y., Ito, H., Fujita, D. & Fujita, M. Permeable self-assembled molecular containers for catalyst isolation enabling two-step cascade reactions. *J. Am. Chem. Soc*. **139**, 6090–6093 (2017).
25. Kiessling, L. L. & Grim, J. C. Glycopolymer probes of signal transduction. *Chem. Soc. Rev*. **42**, 4476–4491 (2013).
26. Sato, S., Ishido, Y. & Fujita, M. Remarkable stabilization of $M_{12}L_{24}$ spherical frameworks through the cooperation of 48 Pd(ii)–pyridine interactions. *J. Am. Chem. Soc*. **131**, 6064–6065 (2009).
27. Murphy, W. L., McDevitt, T. C. & Engler, A. J. Materials as stem cell regulators. *Nat. Mater*. **13**, 547–557 (2014); erratum *Nat. Mater*. **13**, 756 (2014).
28. Chaudhuri, O. et al. Hydrogels with tunable stress relaxation regulate stem cell fate and activity. *Nat. Mater*. **15**, 326–334 (2016).
29. Fuhrmann, A. et al. Conditional repair by locally switching the thermal healing capability of dynamic covalent polymers with light. *Nat. Commun*. **7**, 13623 (2016).
30. Herder, M. et al. Improving the fatigue resistance of diarylethene switches. *J. Am. Chem. Soc*. **137**, 2738–2747 (2015).

**Acknowledgements** We thank the National Science Foundation (CHE-1629358 for J.A.J. and CHE-1506722 for X.L.) for support of this work. This work was supported in part by the MRSEC Program of the National Science Foundation under award number DMR-1419807. Y.G. thanks ExxonMobil for an ExxonMobil–MIT Energy Fellowship. A.P.W. and E.A.A. acknowledge funding from the Research Corporation for Scientific Advancement through a Cottrell Scholars Award. X-ray scattering experiments were performed at the Advanced Photon Source, a US Department of Energy (DOE) Office of Science User Facility operated for the DOE Office of Science by Argonne National Laboratory (DE-AC0206CH11357). We thank G. Clever for discussions.

**Reviewer information** *Nature* thanks S. Sheiko and T. Sirk for their contribution to the peer review of this work.

**Author contributions** Y.G. and J.A.J. conceived the idea. Y.G. designed and conducted the synthesis and characterization studies. E.A.A. and A.P.W. conducted the simulations. H.W. and X.L. conducted the mass spectrometry studies. Y.G. and J.A.J. wrote the manuscript. All authors read and edited the manuscript.

**Competing interests** The authors declare no competing interests.

**Additional information**
**Extended data** is available for this paper at https://doi.org/10.1038/s41586-018-0339-0.
**Supplementary information** is available for this paper at https://doi.org/10.1038/s41586-018-0339-0.
**Reprints and permissions information** is available at http://www.nature.com/reprints.
**Correspondence and requests for materials** should be addressed to J.A.J.
**Publisher's note:** Springer Nature remains neutral with regard to jurisdictional claims in published maps and institutional affiliations.


© 2018 Springer Nature Limited. All rights reserved.

## METHODS

A complete set of detailed synthetic procedures for polymer ligand (PL) and spectral data is available in Supplementary Information.

**Materials and instrumentation.** We purchased all deuterated solvents from Cambridge Isotope Laboratories; 2-chloro-5-methylthiophene from Alfa Aesar; and 4-bromopyridine hydrochloride from Ark Pharm. All other reagents and solvents were purchased from Sigma-Aldrich. Anhydrous, degassed dichloromethane (DCM) and tetrahydrofuran (THF) were used from a J.C. Meyer solvent purification system. High-performance liquid chromatography (HPLC) grade DCM and THF were sparged vigorously with argon for at least one hour before being connected to the solvent purification system. All reactions were performed using standard Schlenk techniques and anhydrous solvents.

UV irradiation was performed with 8 W SANKYO DENKI Blacklight UV lamps with peak emission at 300 nm. Visible light irradiation was performed with four 3-W Sunlite 80146 green LED light bulbs.

All chromatography was performed on EMD Millipore silica gel 60, particle size 0.040–0.063 mm (230–400 mesh), on a Biotage Isolera Prime flash purification system. Gel permeation chromatography (GPC) was performed on an Agilent 1260 LC stack equipped with an Agilent multi-wavelength UV–vis detector, a Wyatt TrEX refractive index detector, a Wyatt DAWN EOS 18-angle light scattering detector and two Shodex KD-806M GPC columns. The GPC system was set to 60 °C at a flow rate of 1 ml $min^{-1}$ with 0.025 M LiBr in DMF. UV–vis spectra were obtained from a Varian Cary 50 Scan UV–vis spectrophotometer.

We acquired $^1$H nuclear magnetic resonance ($^1$H NMR) and $^{13}$C nuclear magnetic resonance ($^{13}$C NMR) spectra on a 500-MHz Varian INOVA spectrometer and processed them in MestReNova 11.0.4. We acquired $^1$H DOSY spectra on the same spectrometer. The gradients were increased from 3.6 G $cm^{-1}$ to 29.2 G $cm^{-1}$ in equally spaced steps using 16 scans. Gradient pulse ($\delta$) was set to 2.0 ms and diffusion time ($\Delta$) set to 0.1 s. Diffusion coefficients for resolved $^1$H signals were extracted from decay curves using the 'peak height fit' in DOSY Transform module of MestReNova 11.0.4.

High-resolution mass spectrometry was done on a Waters quadrupole time-of-flight Premier instrument. Each sample was dissolved by $CH_3CN$ and analysed by direct flow injection (injection volume = 1 μl or 5 μl) electrospray ionization (ESI) in the positive mode. The optimized condition was as follows: ESI capillary voltage 3,000 V, sample cone voltage 35 V, source temperature 120 °C and desolvation temperature 350 °C.

Mass spectrometry of the solution self-assemblies between $Pd^{2+}$ and ligand was recorded with a Waters Synapt G2 spectrometer, using 0.5-mg complex sample in 1 ml of $CH_3CN/CH_3OH$ (3:1, v/v). The following parameters were used: ESI capillary voltage 3.0 kV; sample cone voltage 20 V; extraction cone voltage 0.1 V; source temperature 100 °C; desolvation temperature 100 °C; desolvation gas flow 700 l $h^{-1}$ ($N_2$); sample flow rate 10 μl $min^{-1}$.

Frequency sweep rheology experiments were performed on a TA Instruments Discovery Hybrid Rheometer HR-2. The rheometer was outfitted with an active temperature control system with an environmental enclosure for temperature control. A parallel-plate geometry (radius 8 mm) was used and coupled with a bottom plate, with the typical gap of 1.00 mm between the two plates. Frequency sweep experiments were performed from 1 rad $s^{-1}$ to 100 rad $s^{-1}$ at 0.5% strain, which was first confirmed to be in the linear viscoelastic regime using strain sweep experiments. Shear modulus $G'$ was determined based on $G'$ values at 10 rad $s^{-1}$. Stress-relaxation experiments were carried out at 2% strain. The loaded gel samples were immersed in mineral oil to reduce solvent evaporation and gel de-swelling by adsorbing moisture. The stress relaxation curves were fitted to a stretched exponential function $G = G_0 e^{-(t/\tau)^{\alpha}}$, from which a characteristic relaxation $\tau$ could be obtained[19]. In all the fittings performed, $R^2$ was greater than 0.99.

Transmission SAXS was conducted at beamline 12-ID-B at the Advanced Photon Source at Argonne National Laboratory. The photon energy was 14 keV (that is, wavelength was 0.8857 Å), the beam size was 60 × 200 $\mu m^2$, and the detectors used were Pilatus 2M (SAXS) and Pilatus 300K (wide-angle X-ray scattering WAXS). The sample-to-detector distances were calibrated using silver behenate (AgBe); for the SAXS detector, this was 3,612.22 mm. The exposure time was set to 0.2 s during data collection. A small amount of polyMOCs was removed with a spatula to fill the hole of a circular washer that acted as a sample holder (outer diameter 24 mm, inner diameter 2 mm, thickness 1 mm). To minimize the solvent evaporation on such small-volume samples, the measurement was conducted immediately after the sample was loaded onto the washer.

Swelling measurements were carried out in $CH_3CN$: 0.3 ml of as-formed polyMOC (before or after UV irradiation, 25.1 mM PL concentration) in a 4-ml vial was swollen in $CH_3CN$ at room temperature. After 5 days, the $CH_3CN$ that was not absorbed by the polyMOC was decanted. The inner wall of the vial was carefully wiped to remove the solvent adhering to the wall. The weight of the gel was measured by subtracting the weight of the vial. The polyMOC was further swollen in $CH_3CN$ for 15 days. The same procedure was used to measure its swollen weight at day 20. The swelling ratio was calculated as the ratio between the swollen weight and dry weight, with the latter estimated on the basis of the amount of polymer ligand and $Pd(CH_3CN)_4(BF4)_2$ added during the synthesis of the polyMOC.

**Solution self-assembly of model ligand with $Pd^{2+}$.** We used 1,2-bis(2-methyl-5-(pyridin-4-yl)thiophen-3-yl)cyclopent-1-ene (o-L) as a model compound to study the photo-controlled self-assembly of our non-fluorinated DTE bis-pyridine ligand and $Pd^{2+}$.

To form $Pd_3$(o-L)$_6$ complex, we mixed 2.8 ml o-L solution (4.29 mM in $CD_3CN$) with 0.2 ml $Pd(CH_3CN)_4(BF4)_2$ solution (30.0 mM in $CD_3CN$). On mixing, the solution quickly turned to light green. The mixture was stirred at 70 °C for one hour.

To form the $Pd_{24}$(c-L)$_{48}$ complex, 2.8 ml o-L solution (4.29 mM in $CD_3CN$) was first irradiated with UV light for one hour to form a dark purple solution. $^1$H NMR confirmed that all the o-L was converted to c-L. We then added 0.2 ml $Pd(CH_3CN)_4(BF4)_2$ solution (30.0 mM in $CD_3CN$) to the aforementioned c-L solution. On mixing, the solution quickly turned to dark blue. The mixture was stirred at 70 °C for one hour.

Photoswitching from $Pd_3$(o-L)$_6$ to $Pd_{24}$(c-L)$_{48}$ was performed by irradiating $Pd_3$(o-L)$_6$ solution (2 mM $Pd^{2+}$ concentration in $CD_3CN$) with UV light for 15 h. Photoswitching from $Pd_{24}$(c-L)$_{48}$ to $Pd_3$(o-L)$_6$ was performed by irradiating $Pd_{24}$(c-L)$_{48}$ solution (2 mM $Pd^{2+}$ concentration in $CD_3CN$) with green LED light for 10 h. It should be noted that the conversion from $Pd_3$(o-L)$_6$ to $Pd_{24}$(c-L)$_{48}$ is slow. The same observation was made for an analogous system[23]. These authors postulated that only the small amount of free o-L present at equilibrium in a solution of $Pd_3$(o-L)$_6$ is able to undergo photocyclization. Under gradual but slow shifting of the dynamic equilibrium, the latter reaction delivers the c-L that subsequently reacts with $Pd^{2+}$ to $Pd_{24}$(c-L)$_{48}$.

From DOSY spectra, we measured that the diffusion value ($D$) for $Pd_3$(o-L)$_6$ is $(4.65 \pm 0.51) \times 10^{-10}$ $m^2$ $s^{-1}$, and that for $Pd_{24}$(c-L)$_{48}$ is $(1.94 \pm 0.26) \times 10^{-10}$ $m^2$ $s^{-1}$ (Extended Data Fig. 1c).

To calculate the hydrodynamic radii, we used the Stokes–Einstein equation:

$$r = \frac{kT}{6\pi\eta D}$$

where $r$ is radius, $k$ is Boltzmann constant, $T$ is temperature, $\eta$ is dynamic viscosity of $CD_3CN$ ($3.69 \times 10^{-4}$ Pa $s^{-1}$)[23] and $D$ is diffusion value estimated by the DOSY experiment.

As a result, the hydrodynamic radius was estimated to be 1.27 nm for $Pd_3$(o-L)$_6$ and 3.05 nm for $Pd_{24}$(c-L)$_4$.

**Synthesis of polyMOCs.** *o-gel*. In a 4-ml vial, 49.0 mg o-PL (MW = 5,576) was dissolved in 210 μl $CH_3CN$, to which 90 μl $Pd(CH_3CN)_4(BF4)_2$ solution (97.6 mM in $CH_3CN$) was added. The mixture was vortexed for 20 s before it was annealed at 60 °C for 4 h to obtain the o-gel. Such gels were used for SAXS studies, swelling tests and self-healing tests. To calculate the concentration of PL (or $Pd^{2+}$) in the gels, the volume of poly(ethylene glycol) is taken into account (the density of poly(ethylene glycol) is taken as 1.0 g $cm^{-3}$), and the concentration of PL is thus 25.1 mM.

To prepare samples for shear rheology measurement, the as-mixed gels were transferred to a Teflon mould (8 mm in diameter, 2 mm in height) and sandwiched between two other Teflon sheets assisted by paper clips[19]. The assembly was then heated in an oven at 60 °C for 4 h. A clear circular gel pad was obtained and loaded on the rheometer.

*c-gel*. We prepared a $CH_3CN$ solution of c-PL by UV irradiation of o-PL solution for one hour and no further purification. The c-gel was prepared analogously to the o-gel by replacing o-PL with c-PL.

*o-gel′*. This material was prepared in a similar fashion to the o-gel, with 15% o-PL replaced by o-L (note that each o-PL has two ligands whereas each o-L only has one ligand). The stoichiometry between $Pd^{2+}$ and total amount of ligand was controlled at 1:2.

**Photoswitching between the o-gel and c-gel.** To aid the diffusion of polymer-bound ligands as well as the conversion from $Pd_3$(o-L)$_6$ to $Pd_{24}$(c-L)$_{48}$ (which strongly relies on the dynamics and equilibrium of ligand exchange), the light irradiation was performed at elevated temperature. The o-gel was placed in a closed vial and placed on its side on a digitally controlled hot plate. The surface temperature of the hot plate was set to 60 °C and closely monitored with an infrared thermometer. The conversion from the o-gel to c-gel was achieved in 5 h of UV irradiation. Similarly, when the c-gel was irradiated with green light for 5 h at 60 °C, conversion to the o-gel was achieved. We used 5 h light irradiation at 60 °C in most of this work, except for some of the gels prepared for fatigue studies, for which 12 h light irradiation at 45 °C was used.

For the samples used in shear rheology measurements, the sandwiched-assembly method was again used to prevent the deformation of gel samples. Briefly, the gels were transferred to a Teflon mould (8 mm in diameter, 2 mm in height) and sandwiched between two transparent glass slides assisted by paper clips. The assembly

© 2018 Springer Nature Limited. All rights reserved.

was then placed on a hot plate at 60 °C and was irradiated for 5 h with UV light (or green light).

**SAXS characterization of topology switching.** The high-$q$ regime of the SAXS profile for the c-gel was assigned as the form factor of $Pd_{24}(c\text{-}L)_{48}$, and the peaks were thus fitted with the form factor of a solid spherical particle[31], in which $R$ is the radius of the sphere:

$$P(q) \propto \frac{[\sin(qR) - qR\cos(qR)]^2}{(qR)^6}$$

The fitting results (Extended Data Fig. 3) show that the form factor of a spherical particle with radius 2.9 nm agrees well with the five observed peak positions.

**Simulation method.** Each polymer chain has two ends, and a system's configuration can be expressed as a function of the binding site positions, $\boldsymbol{r}$, and the connectivity between binding site positions via the polymers. Because each binding site is connected to at most one other binding site, the polymer topology connecting binding sites can be expressed as an adjacency vector $\boldsymbol{A}$:

$$\boldsymbol{A} = (A_1, A_2, \ldots, A_{N-1}, A_N)^\top$$

where $N$ is the number of network node binding sites available to the polymer chain ends. If the two ends of a polymer are bound at sites $i$ and $j$, then the sites are connected, and $A_i = j$ and $A_j = i$. It is also possible for one end of a polymer chain to be bound to a network node binding site at a fixed position while the other end of the chain is not bound to a network node (it is not at one of the sites $\in [1, N]$ with a defined position). In this case we define $A_i = 0$. The entropic potential for the polymer chains is the same model for polyethylene glycol described in previous work[5], and the probability for a polymer chain of length $l$ to have an end-to-end distance $r$ is denoted $P_l(r)$.

To sample a network configuration, nodes are generated at random positions within a simulation volume subject only to an excluded volume constraint to prevent nodes from overlapping until a desired system density is reached. Ligand binding site positions are arranged around each node position according to the geometry of the node. Starting with all of the binding positions being available, $a = \{1, \ldots, N\}$, and no connections, $\boldsymbol{A} = \boldsymbol{0}$, available positions are chosen one at a time at random, removed from the list of available positions, and paired with another available binding position (if a viable one exists), which is then also removed from the list of available binding positions. This process continues until all the binding sites at network nodes have been paired up (except in cases when no viable pair exists). The probability that the ligand on one end of a polymer chain will bind at position $\boldsymbol{r}_j$ given that the ligand on the other end is at position $\boldsymbol{r}_i$ is proportional to the probability of the free polymer of length $l$ having an end-to-end distance $r_{ij}$. The probability of position $i$ pairing with available position $j$ (assuming there is at least one viable pair available to $i$) is:

$$P(A_i = j) = \frac{P_l(r_{ij})}{\sum_{k \in a} P_l(r_{ik})} \quad \text{if } \exists\, k \in a \text{ such that } P_l(r_{ik}) > 0$$

Simulations used a cubic, fully periodic simulation cell with side lengths of 100 nm, containing 16,154 pairs of connected ligands mediated by a polymer potential parameterized for polyethylene glycol with 100 repeat units. The network nodes for a given simulation comprised 4, 6, 12, 24 or 48 binding positions arranged in the $Pd_2L_4$, $Pd_3L_6$, $Pd_6L_{12}$, $Pd_{12}L_{24}$ or $Pd_{24}L_{48}$ geometry, respectively. Results were averaged over 100 independent simulations for each set of conditions. In all the simulations performed, the concentration of $Pd^{2+}$ was set to 25.1 mM and the stoichiometry between $Pd^{2+}$ and PL was set to 1:1 (that is, $[Pd^{2+}]:[L] = 1:2$), which is consistent with the experimental condition.

**Phantom-to-affine network transition through topology switching.** Along with the increase in primary loops described in main text, simulation results indicate that the ultra-high functionality of the c-gel leads to an abundance of secondary loops (Extended Data Fig. 5b), wherein two MOCs are bridged by two or more strands. Unlike primary loops, which are elastically inactive, secondary loops do contribute to elasticity; however, the extent of their contribution depends on which theoretical model network is considered (for example phantom or affine network)[17,32]. To address which theory was more appropriate to describe each topological state of our material, we calculated the average total number of connections per MOC ($\overline{f}_{tc}$, an affine model-based approximation for $\overline{f}$; Extended Data Fig. 5c) and the average number of active connections (where secondary loops are treated as one effective connection; Extended Data Fig. 5d) per MOC ($\overline{f}_{ac}$, a phantom model-based approximation), as a function of MOC stoichiometry for a range of simulated polyMOCs (Extended Data Fig. 6). We found that for polyMOCs derived from small MOCs, for example the o-gel, the difference between $\overline{f}_{tc}$ and $\overline{f}_{ac}$ is almost negligible. In contrast, the large number of secondary loops in the c-gel leads to an $\overline{f}_{tc}$ value that is three times larger than $\overline{f}_{ac}$. We postulated that in the c-gel topological state, the high density of polymer chains attached to each $Pd_{24}L_{48}$ junction may suppress junction fluctuations, which would lead to affine network behaviour. Moreover, junction fluctuations in the o-gel state would be best captured by the phantom network model[5,17]. In other words, our photoswitchable polyMOC could behave as two fundamentally different networks depending on its topological state.

This hypothesis was supported by our rheological data. Measured $G'$ values for the o-gel and c-gel were used to calculate $\overline{f}_{affine}$ and $\overline{f}_{phantom}$ (see Supplementary Information). As shown in Extended Data Fig. 6, $\overline{f}_{phantom}$ agrees well with $\overline{f}_{ac}$ for the o-gel. In contrast, $\overline{f}_{affine}$ shows excellent agreement with $\overline{f}_{tc}$ for the c-gel.

**Fatigue studies.** To study the fatigue properties of polyMOCs over switching cycles, we prepared several samples of the o-gel using the sandwiched-assembly method, where the circular gel in a Teflon mould was sandwiched between two transparent glass slides and annealed. Each o-gel was irradiated alternately with UV light and green light for several cycles (from zero to seven cycles) at 60 °C (each irradiation took 5 h) or 45 °C (each irradiation took 12 h). The polyMOC was then taken out of the mould and subjected to rheological or SAXS measurements. For each data point, averages and standard deviations were computed for three trials. To avoid the deformation of samples or solvent loss, samples were not re-used after measurements (that is, if seven switching cycles were examined, a total of $15 \times 3$ gel samples were made using the sandwiched-assembly method).

To simulate the fatigue behaviours, we set a certain fraction of the ligand as inactive as a starting parameter, then simulated the polyMOC self-assembly process and obtained the average branch functionality in the equilibrium stage. Given the postulation that the o-gel adopts phantom network behaviour while the c-gel adopts affine network behaviour, the simulated branch functionality for the o-gel is based on active connections (Extended Data Fig. 7a) and for the c-gel is based on total connections (Extended Data Fig. 7b).

From our study on the small-molecule ligand (Extended Data Fig. 8), about 80% of the ligand is still active after 18 h of UV irradiation. On the other hand, after seven switching cycles, the polyMOC has been exposed to UV irradiation for 35 h in total. We postulate that the fatigue behaviour of our polyMOCs is mainly dictated by UV-induced side reactions of DTE.

**Data availability.** The data that support the findings of this study are available from the corresponding author on reasonable request.

31. Pedersen, J. S. Analysis of small-angle scattering data from colloids and polymer solutions: modeling and least-squares fitting. *Adv. Colloid Interface Sci.* **70**, 171–210 (1997).
32. Lang, M. Elasticity of phantom model networks with cyclic defects. *ACS Macro Lett.* **7**, 536–539 (2018).

© 2018 Springer Nature Limited. All rights reserved.

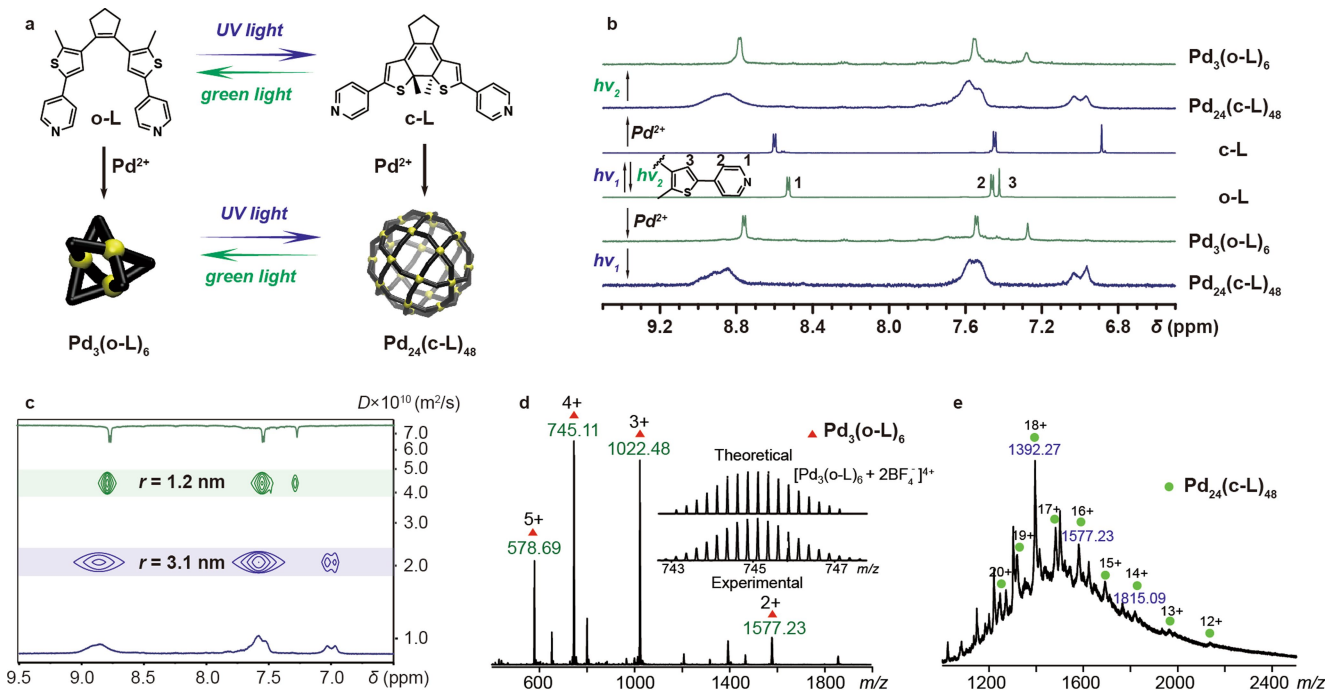


**Extended Data Fig. 1 | Solution self-assembly of DTE-based bis-pyridine ligand and $Pd^{2+}$. a**, DTE-containing bis-pyridine photoswitch reversibly interconverts between open (o-L) and closed (c-L) forms. Note that the ring-closure reaction produces *trans*-isomers (racemic). In the presence of $Pd^{2+}$, o-L and c-L form $Pd_3(o\text{-}L)_6$ and $Pd_{24}(c\text{-}L)_{48}$ MOCs, which can be interconverted using light. **b**, Aromatic regions of the solution $^1$H NMR spectra ($CD_3CN$, 25 °C, $\omega/2\pi = 500$ MHz) for o-L and c-L, and corresponding MOCs prepared from these ligands and $Pd(CH_3CN)_4(BF_4)_2$. Photoswitching steps are indicated by black arrows. **c**, $^1$H DOSY measurements indicate that $Pd^{2+}$ forms a smaller assembly with o-L (green spectrum) and a larger assembly with c-L (blue spectrum). From a series of $^1$H NMR spectra generated from $^1$H DOSY measurements, the decay of peak intensities was fitted to provide the diffusion value ($D$) for $Pd_3(o\text{-}L)_6$ (green shaded region) and $Pd_{24}(c\text{-}L)_{48}$ (blue shaded region), respectively. From the measured diffusion values, the hydrodynamic radii of $Pd_3(o\text{-}L)_6$ and $Pd_{24}(c\text{-}L)_{48}$ were calculated. **d**, ESI mass spectrum of $Pd_3(o\text{-}L)_6$. The charge states of intact assemblies due to the loss of counterions are marked. Inset shows the simulated and observed isotopic patterns of $[Pd_3(o\text{-}L)_6 + 2BF_4^-]^{4+}$. **e**, Cold spray ionization mass spectrum of $Pd_{24}(c\text{-}L)_{48}$. The charge states of intact assemblies due to the loss of counterions are marked.

© 2018 Springer Nature Limited. All rights reserved.

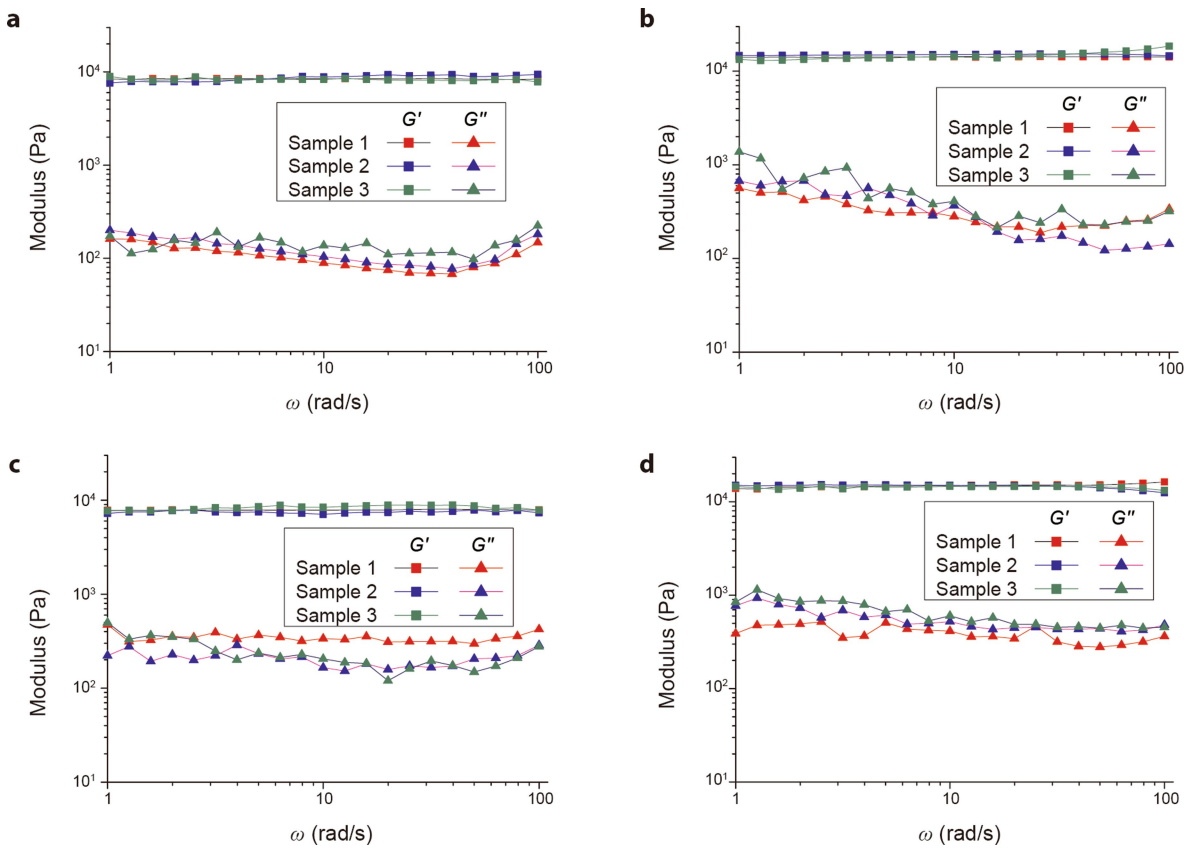


**Extended Data Fig. 2 | Frequency sweeps in oscillatory rheometry at 0.5% strain. a**, Data for three o-gel samples. **b**, Data for three o-gel samples after UV irradiation. **c**, Data for three o-gel samples after UV irradiation followed by green-light irradiation. **d**, Data for three c-gel samples prepared directly from c-PL.

© 2018 Springer Nature Limited. All rights reserved.

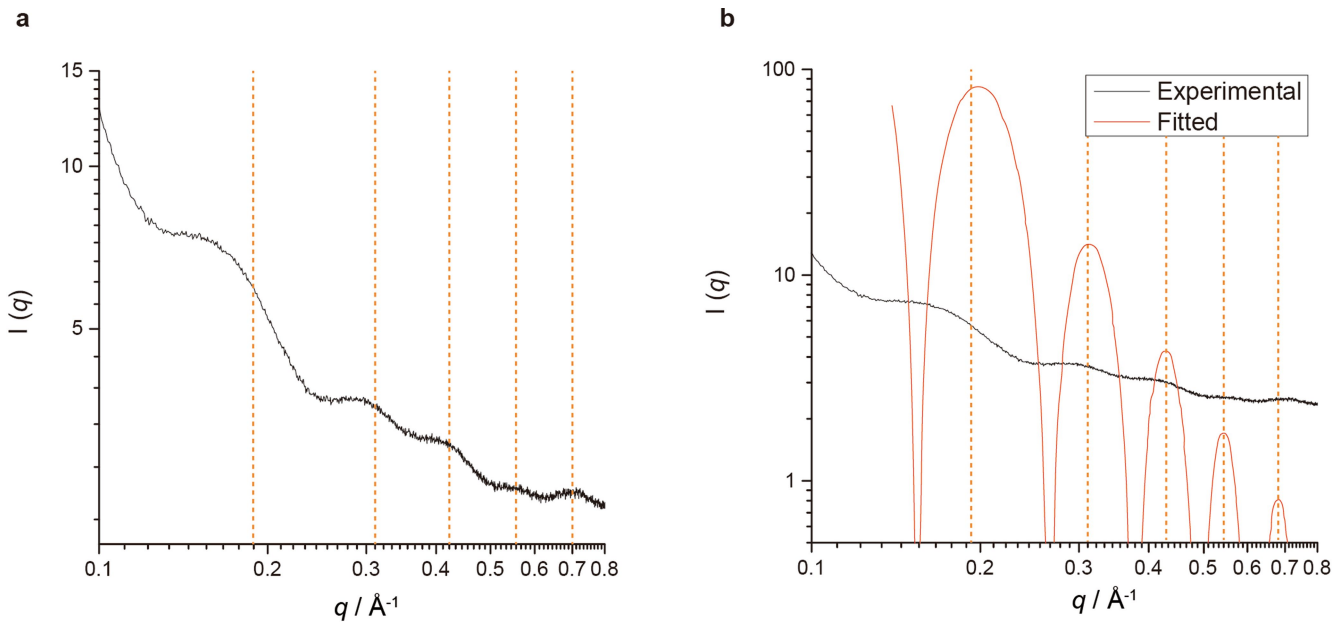


**Extended Data Fig. 3 | Fitting of high-*q* SAXS profile of the c-gel. a**, High-*q* regime of the SAXS profile for the c-gel. Five peaks were identified (dashed lines) and indexed. **b**, Experimental results were fitted with the form factor of a spherical particle with radius 2.9 nm.

© 2018 Springer Nature Limited. All rights reserved.

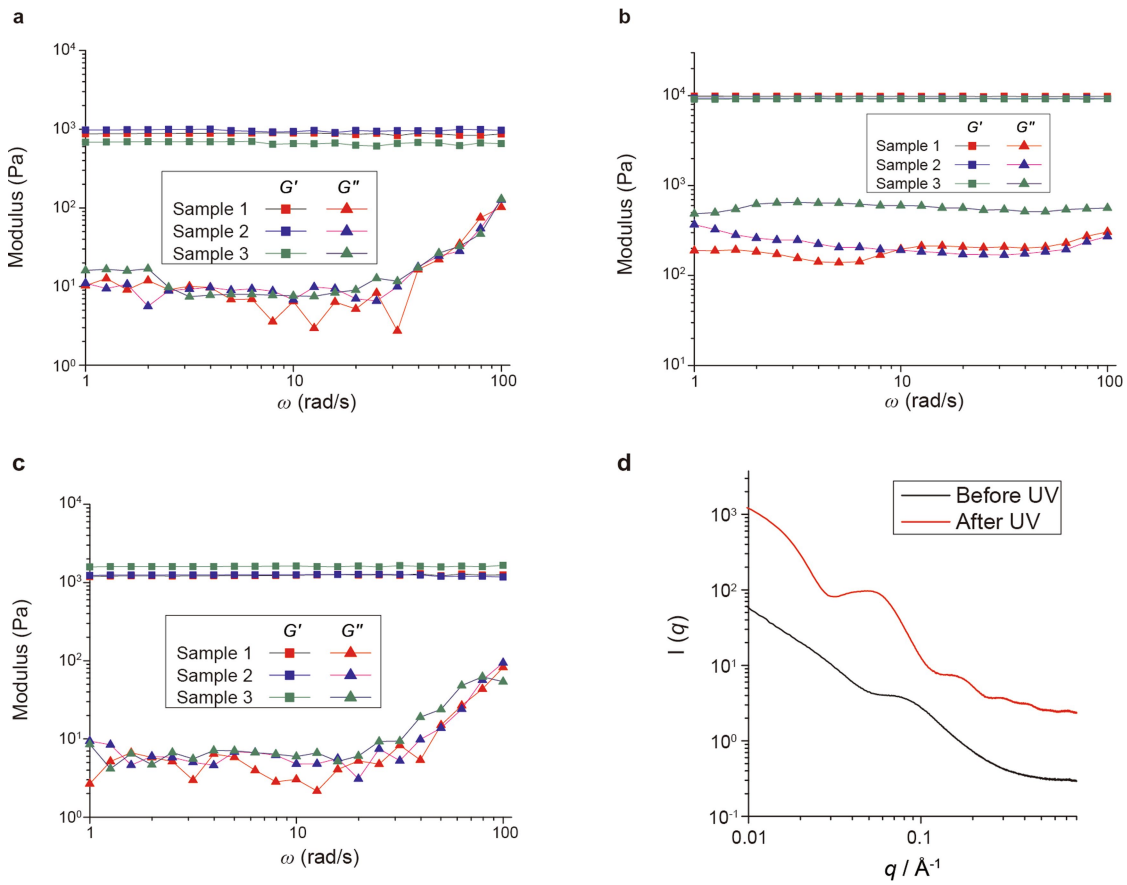


**Extended Data Fig. 4 | Topology switching in the presence of free ligand as defects. a**, Frequency sweep in oscillatory rheometry at 0.5% strain for three o-gel′ samples. **b**, Frequency sweep in oscillatory rheometry at 0.5% strain for three o-gel′ samples after UV irradiation. **c**, Frequency sweep in oscillatory rheometry at 0.5% strain for three o-gel′ samples after UV irradiation followed by green-light irradiation. **d**, SAXS curves for the o-gel′ before and after UV irradiation.

© 2018 Springer Nature Limited. All rights reserved.

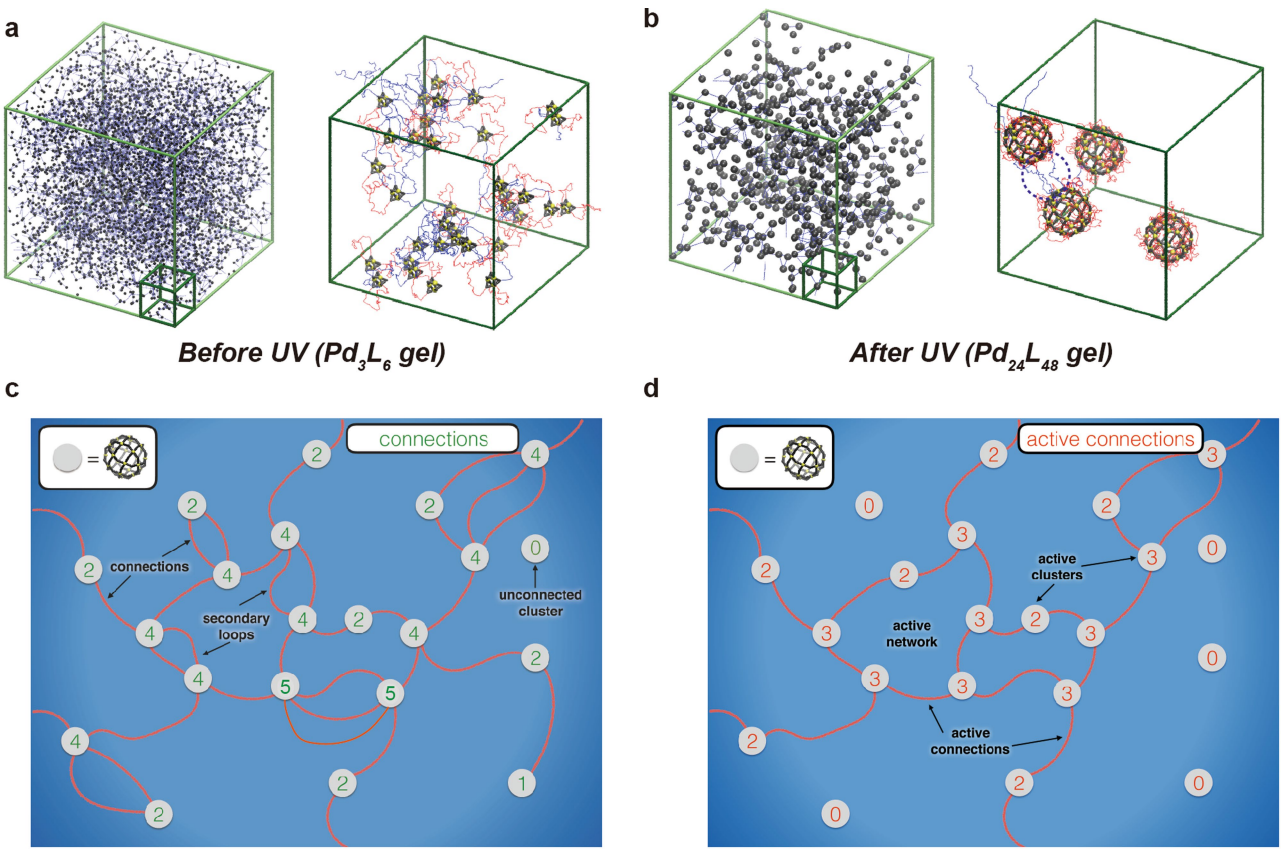


**Extended Data Fig. 5 | Simulations of network topology. a**, Snapshots of in silico polyMOCs before UV irradiation. Left: MOC junctions are shown as grey spheres and polymer chains connecting MOC junctions are shown in blue. Right: A zoom-in view of the region in the green cube in the left panel. Looped and non-looped polymer chains are shown in red and blue, respectively. **b**, Snapshots of in silico polyMOCs after UV irradiation. Left, MOC junctions are shown as grey spheres, and polymer chains connecting MOC junctions are shown in blue. Right, A zoom-in view of the region in the green cube in the left panel. Looped and non-looped polymer chains are shown in red and blue, respectively. The blue dashed circle shows a representative case in which two $Pd_{24}L_{48}$ clusters are connected by multiple polymer chains (that is, multiple secondary loops). **c**, A representative polymer network which is abundant in secondary loops. The connectivity of each junction is calculated on the basis of the total connections, which describes the number of polymer chains connecting MOCs. **d**, The same polymer network is represented in another way by calculating the connectivity of each junction on the basis of the active connections.

© 2018 Springer Nature Limited. All rights reserved.

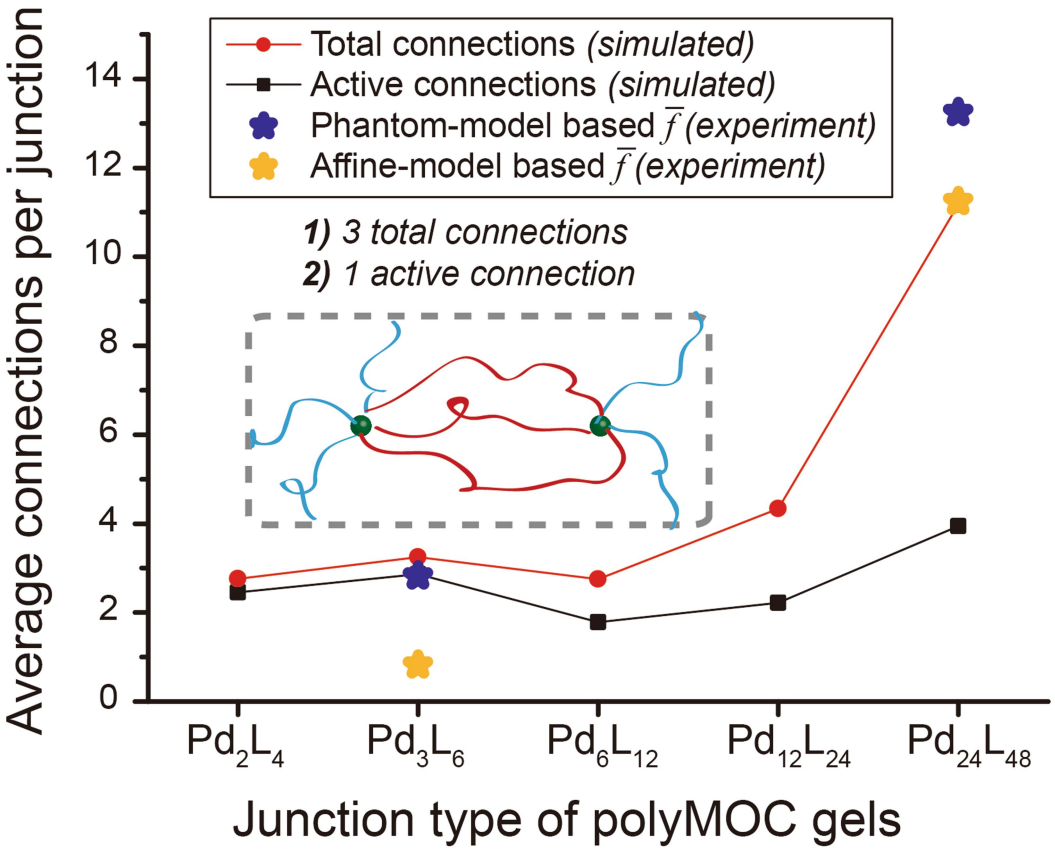


**Extended Data Fig. 6 | Simulated results for average connections per MOC for a series of polyMOCs with various $Pd_xL_y$ stoichiometries.** Two types of connections between MOCs are defined: total connections and active connections. These connections correspond to two classical models of elasticity: the affine model (total connections, red curve) and the phantom model (active connections, black curve). Both affine (yellow stars) and phantom (blue stars) models were used to calculate the average branch functionality for the o-gel and c-gel based on measured $G'$, and the results were compared with simulated active connections and total connections. For the o-gel, the phantom-model based experimental calculation agrees well with simulated active connections; for the c-gel, the affine-model based experimental calculation agrees well with simulated total connections. The experimental and simulated results suggest that the o-gel is best described as a phantom network while the c-gel is best described as an affine network.

© 2018 Springer Nature Limited. All rights reserved.

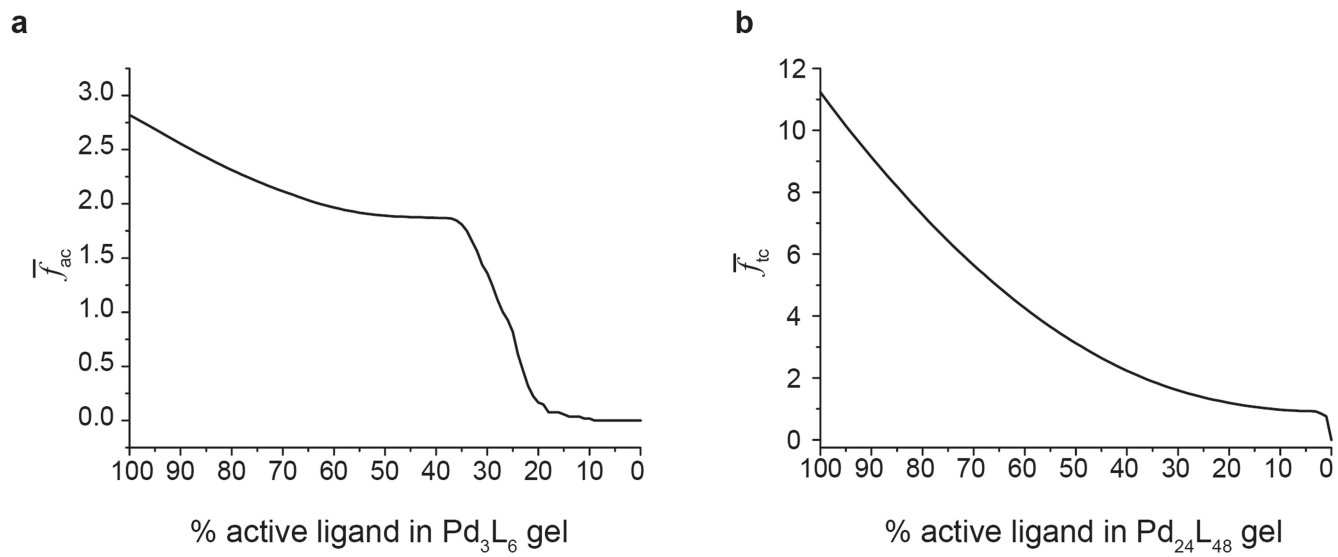


**Extended Data Fig. 7 | Simulation studies of fatigue behaviours. a**, Simulation results for $\overline{f}_{ac}$ of $Pd_3L_6$ gel obtained by assuming that a certain fraction of ligand is inactive. **b**, Simulation results for $\overline{f}_{tc}$ of $Pd_{24}L_{48}$ gel obtained by assuming that a certain fraction of ligand is inactive.

© 2018 Springer Nature Limited. All rights reserved.

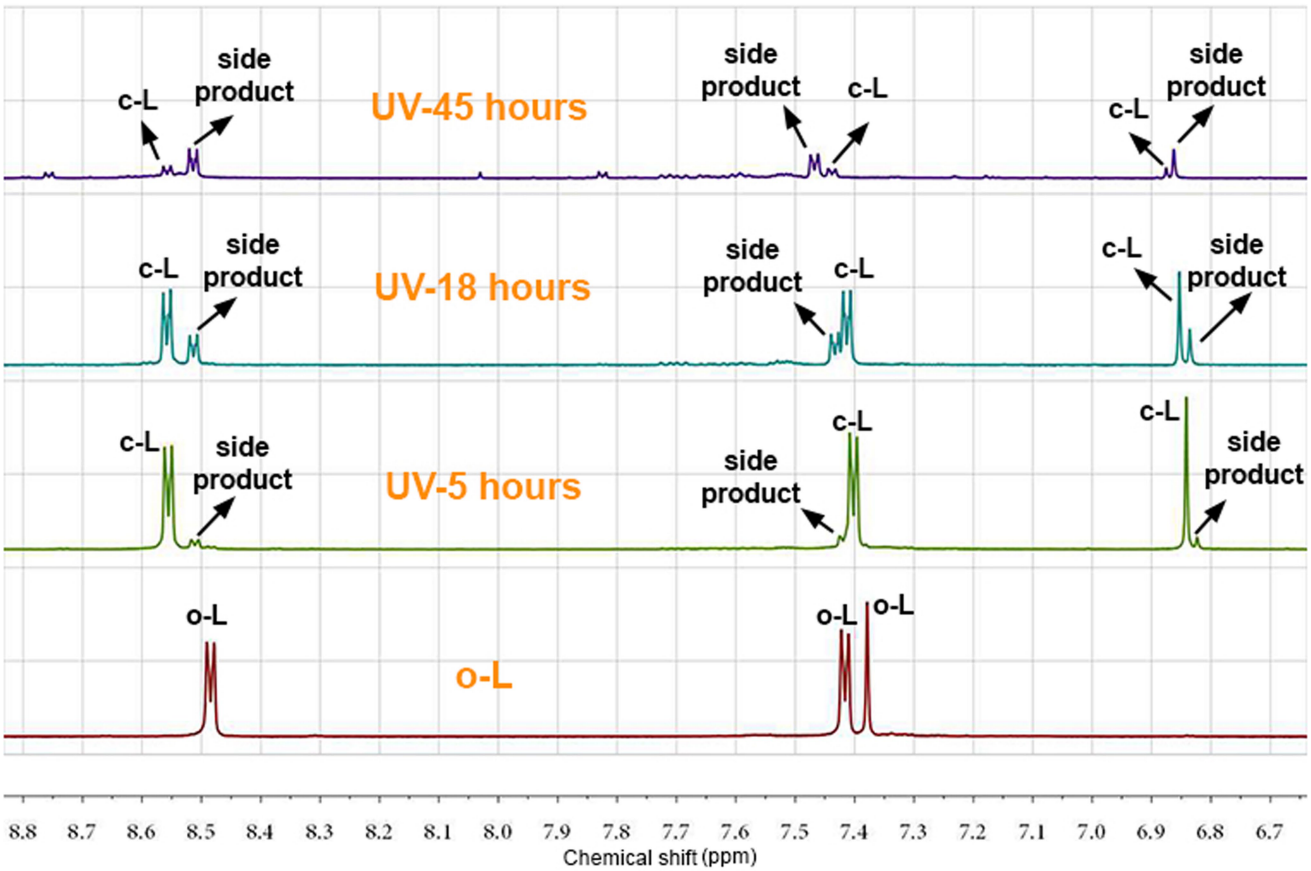


**Extended Data Fig. 8 | $^{1}$H NMR of the aromatic regions of model compound o-L during UV irradiation.** The o-L was completely converted to c-L after 5 h, with approximately 2% side product as indicated by the presence of a second set of peaks. After 18 h of UV irradiation, about 20% of c-L was converted to the side product. By 45 h, more than 80% of the c-L had undergone side reaction(s).

© 2018 Springer Nature Limited. All rights reserved.